GEOPHYSICS, VOL. 80, NO. 4 (JULY-AUGUST 2015); P. S127–S136, 17 FIGS.
10.1190/GEO2014-0453.1

CrossMark
click for updates

Downloaded 08/11/16 to 138.67.12.184. Redistribution subject to SEG license or copyright; see Terms of Use at http://library.seg.org/

Scalar imaging condition for elastic reverse time migration

Yuting Duan[1] and Paul Sava[1]

ABSTRACT

Polarity changes in converted-wave images constructed by elastic reverse time migration cause destructive interference after stacking over the experiments of a seismic survey. This polarity reversal is due to PS and SP reflectivities reversing sign at certain incidence angles, e.g., at normal incidence in isotropic media. Many of the available polarity correction methods are complex and require costly transformations, e.g., to the angle domain. We derive a simple imaging condition for converted waves to correct the image polarity and reveal the conversion strength from one wave mode to another. Our imaging condition exploits pure P- and S-modes obtained by Helmholtz decomposition. Instead of correlating Cartesian components of the vector S-mode with the P-mode, we exploit all three components of the S wavefield at once to produce a unique image. We generate PS and SP images using geometric relationships among the propagation directions for the P- and S-wavefields, the reflector orientation, and the S-mode polarization direction. Compared with alternative methods for correcting the polarity reversal of PS and SP images, our imaging condition is simple and robust and does not significantly increase the cost of reverse time migration. Several numerical examples were used to test the effectiveness of our new imaging condition using simple and complex models.

INTRODUCTION

Advances in seismic acquisition and ongoing improvements in computational capability have made imaging using multicomponent elastic waves increasingly feasible. Elastic migration with multicomponent seismic data can provide additional subsurface structural information compared with conventional acoustic migration using single-component data. Multicomponent seismic data can be used, for example, to estimate fracture distributions as well as elastic properties. Such data can also provide broader illumination of the subsurface, thus reducing potential P-wave shadow zones.

In complex geologic environments, it is desirable to use wavefield-based imaging methods, e.g., reverse time migration (RTM). Conventional RTM consists of two steps: wavefield extrapolation followed by the application of an imaging condition (Claerbout, 1971). Wavefield extrapolation requires constructing source and receiver wavefields using an estimated wavelet and the recorded data, respectively. In elastic media, source and receiver wavefields are constructed using different forms of elastic (vector) wave equations corresponding to different parameterizations of the subsurface model parameters.

Following wavefield extrapolation, an imaging condition is applied by combining the source and receiver wavefields to obtain images of subsurface structures. Multicomponent wavefields allow for a variety of imaging conditions (Denli and Huang, 2008; Yan and Sava, 2008; Artman et al., 2009; Wu et al., 2010). A simple imaging condition for multicomponent wavefields is the crosscorrelation of the Cartesian components of the displacement vectors characterizing the source and receiver wavefields (Yan and Sava, 2008). In 3D, this results in nine images for different combinations of source and receiver displacement vector components. One limitation of this method is that the P- and S-modes are mixed in the extrapolated wavefields; therefore, crosstalk between P- and S-modes creates artifacts that make interpretation difficult. Another imaging condition for multicomponent wavefields first requires the decomposition of wavefields into different wave modes, for example, P- and S-modes. For isotropic elastic wavefields far from the source, the P- and S-modes correspond to the compressional and transverse components of the wavefield, respectively (Aki and Richards, 2002). Similar to the imaging condition using displacement vector components, this imaging condition provides multiple images by crosscorrelating different wave modes present in the source and receiver wavefields (Dellinger and Etgen, 1990; Yoon et al., 2004; Yan and Sava, 2008; Yan and Xie, 2012). However, in this case, images correspond to reflectivity for different combinations of incident and reflected P- and S-modes, e.g., PP, PS, SP, and SS

Manuscript received by the Editor 25 September 2014; revised manuscript received 11 January 2015; published online 18 June 2015.
[1]Colorado School of Mines, Center for Wave Phenomena, Golden, Colorado, USA. E-mail: yduan@mymail.mines.edu; psava@mines.edu.
© 2015 Society of Exploration Geophysicists. All rights reserved.

Downloaded 08/11/16 to 138.67.12.184. Redistribution subject to SEG license or copyright; see Terms of Use at http://library.seg.org/

reflectivity, and therefore they are more useful in geologic interpretation.

One difficulty when imaging multicomponent wavefields is that the PS and SP images change sign at certain incidence angles. For example, in isotropic media, polarity reversal occurs at normal incidence (Balch and Erdemir, 1994). This sign change can lead to destructive interference when multiple experiments of a seismic survey are stacked for a final image. A simple way to correct the polarity reversal in PS and SP images is based on the assumption that the polarity change occurs at zero offset and can be corrected based on the acquisition geometry. However, this assumption fails if the reflectors are not horizontal (Du et al., 2012b). An alternative method to correct for the polarity change requires that we compute the incidence angles at each image point and then reverse the polarity based on this estimated angle under the assumption that the polarity reverses at normal incidence. There are various techniques to compute the reflection angles. One possibility is to use ray theory to simulate the incident wavefield direction and apply this direction to the reflected wave extrapolated from the surface to every imaging point (Balch and Erdemir, 1994). This method is limited by the ray approximation and may become impractical when applied to elastic RTM in media characterized by complex multipathing. Another method to correct for polarity changes is to image in the angle domain and then reverse the image polarity as a function of angle (Rosales et al., 2008; Yan and Sava, 2008; Yan and Xie, 2012). Constructing angle-domain common image gathers is accurate and robust, but it can also be expensive. Finally, another possibility for polarity correction is to reverse the polarity in the source and receiver wavefields based on the sign of the reflection coefficient, which is computed from the directions of the incident and reflected waves (Sun et al., 2006; Du et al., 2012a). These directions are typically computed using Poynting vectors, which may be inaccurate in complicated models characterized by multipathing (Dickens and Winbow, 2011; Patrikeeva and Sava, 2013).

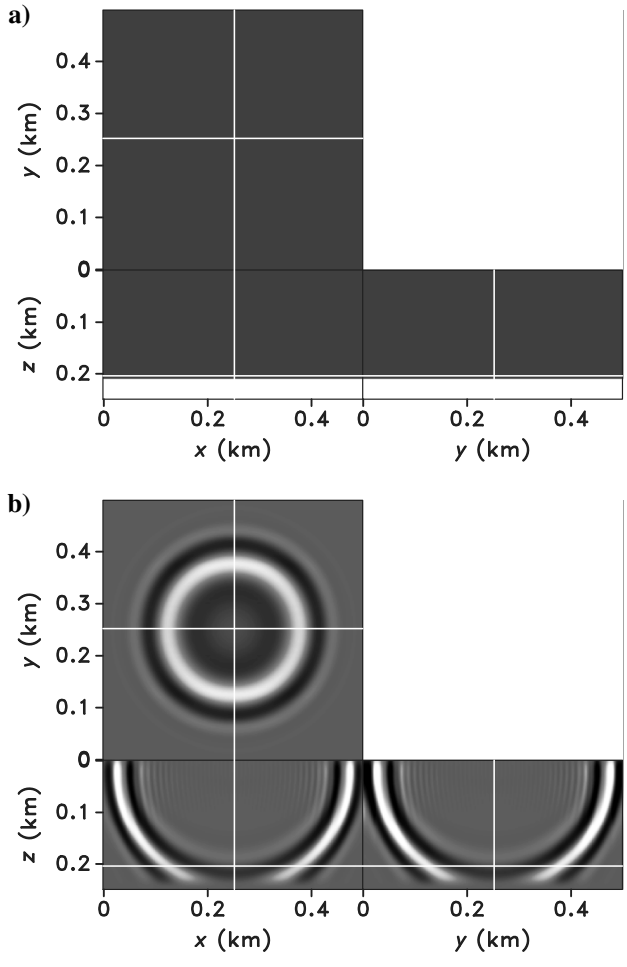


Figure 1. (a) 3D synthetic model with one horizontal reflector in a constant-velocity medium, at depth $z = 0.2$ km. The source is located at (0.2, 0.2, 0.02) km; the 2D network of receivers is at $z = 0.03$ km. (b) A snapshot of the source P wavefield.

In this paper, we propose an alternative 3D imaging condition for elastic RTM. Our new imaging condition exploits geometric relationships among incident and reflected wave directions, reflector orientation, and rotation directions of S wavefields . Using our new imaging condition, we are able to obtain PS and SP images without polarity reversal. The method is simple and robust and operates on separated wave modes obtained, for example, using Helmholtz decomposition (Yan and Sava, 2008). Our method is also computationally efficient to apply because it does not require complex operations such as angle or directional decomposition. We begin by discussing the theory underlying our method and then illustrate it using simple and complex synthetic examples.

THEORY

Our proposed imaging condition is meant to automatically compensate for the polarity reversal characterizing conventional converted-wave images. Our method builds on existing techniques that first decompose elastic wavefields into pure P- and S-modes. However, in contrast with more conventional methods, our imaging condition does not correlate the P-mode with different components of the vector S-mode. We explain the logic of our method next.

Reconstructed source and receiver elastic wavefields can be separated into P- and S-modes prior to imaging (Dellinger and Etgen, 1990; Yan and Sava, 2008). In isotropic media, this separation can be performed using Helmholtz decomposition (Aki and Richards, 2002), which describes the compressional component P and transverse component $\mathbf{S}$ of the wavefield using the divergence and curl of the displacement vector field $\mathbf{u}$:

$$P(e, \mathbf{x}, t) = \nabla \cdot \mathbf{u}(e, \mathbf{x}, t), \tag{1}$$

$$\mathbf{S}(e, \mathbf{x}, t) = \nabla \times \mathbf{u}(e, \mathbf{x}, t). \tag{2}$$

Wavefields $\mathbf{u}$, P, and $\mathbf{S}$ are functions of the experiment index e, space $\mathbf{x}$, and time t. PS and SP images can then be obtained by crosscorrelating the P wavefield with each component of the $\mathbf{S}$ wavefield (Yan and Sava, 2008). Images produced in this way have three independent components at every location in space; i.e., the PS and SP images are vector images. The method discussed here is applicable to wavefields reconstructed in isotropic media, but it can be adapted to anisotropic media, for example, by using the method discussed by Yan and Sava (2008).

We illustrate this conventional imaging condition with the 3D synthetic model shown in Figure 1a, which contains one horizontal reflector embedded in a constant-velocity medium. A single

pressure source is at (0.2, 0.2, 0.02), and the source function is a Ricker wavelet with a peak frequency of 30 Hz. Figure 1b shows a snapshot of the source P-wavefield for a single source indicated in Figure 1a. The *x*-, *y*-, and *z*-components of the receiver S-wavefield are shown in Figure 2a, 2c, and 2e, respectively. P- and S-wavefields are decomposed from the displacement wavefield using Helmholtz decomposition. The *z*-component of the receiver S-wavefield corresponds to S-waves propagating in the *xy*-plane,

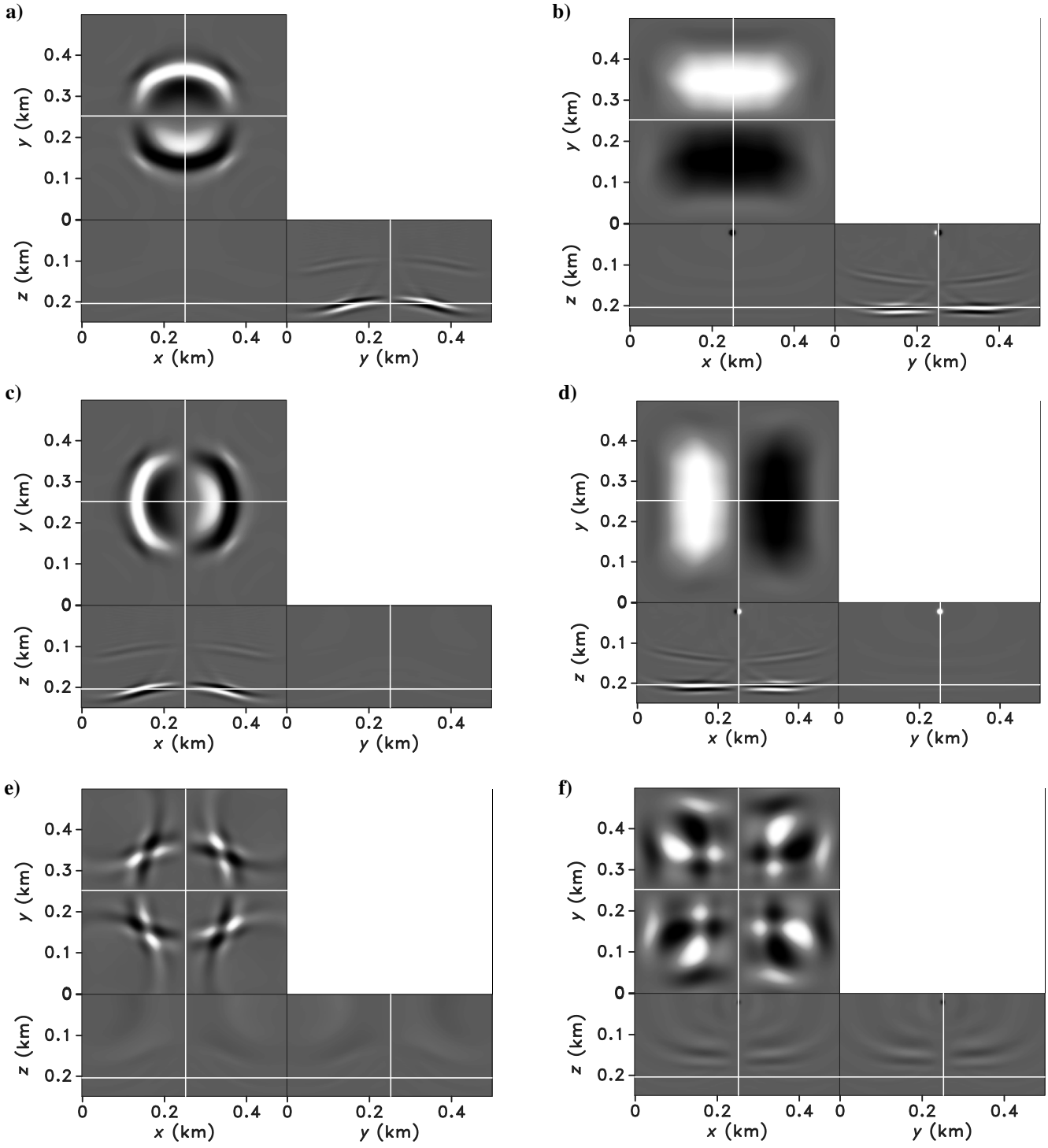


Figure 2. Snapshots of the (a) *x*- (c) *y*-, and (e) *z*-components of the receiver S-wavefield and the corresponding (b) *x*- (d) *y*-, and (f) *z*-components of the PS image. The S-wavefields are decomposed from the displacement wavefield using Helmholtz decomposition. Polarity reversal occurs as a function of azimuth in the wavefield, which leads to polarity change in three components of the PS image shown. The *z*-component of the S-wavefield is much weaker than the *x*- and *y*-components.

Downloaded 08/11/16 to 138.67.12.184. Redistribution subject to SEG license or copyright; see Terms of Use at http://library.seg.org/

Downloaded 08/11/16 to 138.67.12.184. Redistribution subject to SEG license or copyright; see Terms of Use at http://library.seg.org/

which are weaker than the x- and y-component shown in 2e. In Figure 2a and 2c, another S-wave appearing at $z = 0.1$ km is converted from P-waves in the recorded data. Such waves produce artifacts in the migrated images, as seen in Figure 2b, 2d, and 2f. Because the artifacts are generally inconsistent with each other between different shots, they are attenuated in stacked images (Duan and Sava, 2014). Notice that polarity reversal occurs as a function of the azimuth, which leads to the polarity change in the three components of the PS image shown in Figure 2b, 2d, and 2f.

Another problem of the conventional imaging condition is that it is difficult to find the physical meaning of the various constructed images. We seek to avoid vector PS and SP images by combining all components of the S-wavefield with the P-wavefield into a single image representing the energy conversion strength from one wave mode to another at an interface.

To formulate the imaging condition, we define the following quantities, shown in Figure 3:

- vectors $\mathbf{D}_P$ and $\mathbf{D}_S$ indicating the propagation directions of an incident P-wave and the corresponding reflected SV-wave, respectively
- vector $\mathbf{n}$ indicating the direction normal to the interface plane $\mathcal{I}$
- vector $\mathbf{S}$ indicating the S-mode rotation direction, i.e., $\nabla \times \mathbf{u}(e, \mathbf{x}, t)$

The vector $\mathbf{S}$ wavefield contains SV-waves as well as SH-waves; therefore, the receiver wavefield vector $\mathbf{S}$ is not, in general, orthogonal to plane $\mathcal{R}$, and it can be decomposed into vectors $\mathbf{S}_\perp$ and $\mathbf{S}_\parallel$ such that

$$\mathbf{S} = \mathbf{S}_\perp + \mathbf{S}_\parallel. \tag{3}$$

Vectors $\mathbf{S}_\perp$ and $\mathbf{S}_\parallel$ are orthogonal and parallel to plane $\mathcal{R}$, respectively. The SV-waves reflected from incident pure P-waves are confined to the vector field $\mathbf{S}_\perp$ because the displacement wavefield for SV-waves is in plane $\mathcal{R}$. According to Snell's law, vectors $\mathbf{D}_P$, $\mathbf{D}_S$, and $\mathbf{n}$ belong to the reflection plane $\mathcal{R}$. Vector $\mathbf{S}_\perp$ is orthogonal to vector $\mathbf{D}_S$. Note that we never compute vectors $\mathbf{D}_P$ and $\mathbf{D}_S$; we only use them to help explain our imaging condition. A similar explanation is applicable to SP reflections.

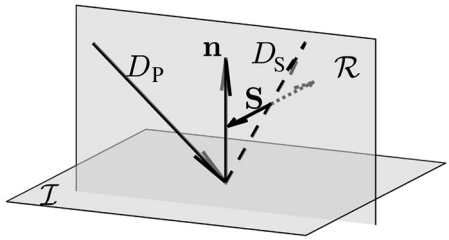


Figure 3. Schematic description of wave propagation in 3D media. The vectors in the solid and dashed lines denote the incident P and the reflected S-waves, respectively. Vector $\mathbf{n}$ indicates the normal to the interface $\mathcal{I}$, and vectors $\mathbf{D}_P$ and $\mathbf{D}_S$ indicate the propagation directions of the incident P-mode and of the reflected S-mode, respectively. Vectors $\mathbf{D}_P$, $\mathbf{D}_S$, and $\mathbf{n}$ are all contained in the reflection plane $\mathcal{R}$. Vector $\mathbf{S}$ is the curl of the wavefield. If we only consider the reflected SV-wave, $\mathbf{S}$ represents the polarization of the reflected SV-wave, which is orthogonal to plane $\mathcal{R}$.

As indicated earlier, the signs of the PS and SP reflection coefficients change across normal incidence in every plane, which causes the polarity of the reflected waves to change at normal incidence. Because normal incidence depends on the acquisition geometry and the geologic structure, this polarity reversal can occur at different positions in space, thus making it difficult to stack images for an entire multicomponent survey.

To address this challenge, we propose new scalar imaging conditions for PS and SP images:

$$I^{\mathrm{PS}}(\mathbf{x}) = \sum_e \sum_t (\nabla P(e, \mathbf{x}, t) \times \mathbf{n}(\mathbf{x})) \cdot \mathbf{S}(e, \mathbf{x}, t), \tag{4}$$

$$I^{\mathrm{SP}}(\mathbf{x}) = \sum_e \sum_t ((\nabla \times \mathbf{S}(e, \mathbf{x}, t)) \cdot \mathbf{n}(\mathbf{x})) P(e, \mathbf{x}, t). \tag{5}$$

Here, P and $\mathbf{S}$ are functions of the experiment index e, space $\mathbf{x}$ and time t, and represent the scalar P- and vector S-modes after Helmholtz decomposition, respectively. $I^{\mathrm{PS}}(\mathbf{x})$ and $I^{\mathrm{SP}}(\mathbf{x})$ are the PS and SP scalar images, respectively. This expression contains summation over time as well as summation over experiments. We assume that we know the normal vector $\mathbf{n}$, which can be obtained in practice, for example, from a prior computed PP image. Note that waves with small incidence angles contribute to PS and SP images much less than those with larger incidence angles because the PS and SP reflectivities approach zero as the incidence angle decreases to zero. Thus, a small error in the estimation of normal vector $\mathbf{n}$ would affect only the polarity correction at small incidence angles, and this effect can be neglected in the stacked image. In fact, for the examples shown in this paper, we use a smoothed version of the true normal vectors and obtain satisfactory results.

The physical interpretations of our new scalar imaging condition (equations 4 and 5) is as follows:

- *PS imaging* (equation 4): We interpret vector ∇P as the propagation direction of the P-mode, which can be calculated directly on the separated P wavefield. The crossproduct with the normal vector $\mathbf{n}$ constructs a vector orthogonal to the reflection plane $\mathcal{R}$; as indicated earlier, this direction is parallel to the rotation direction of the S-mode, $\mathbf{S}_\perp$. Therefore, the dot product of $\nabla P \times \mathbf{n}$ and $\mathbf{S}$ is just a projection of the vector S wavefield onto a direction that depends on the incidence direction of the P-wavefield. For a P-mode incident in the opposite direction, the vector $\nabla P \times \mathbf{n}$ reverses direction, thus compensating for the opposite polarization of the S-mode. Consequently, the PS imaging condition has the same sign regardless of incidence direction, and therefore PS images can be stacked without canceling each other at various positions in space.
- *SP imaging* (equation 5): We interpret the vector $\mathbf{S}$ as the rotation direction of the S-mode, and for the situation considered here, it is orthogonal to the reflection plane $\mathcal{R}$. Therefore, vector $\nabla \times \mathbf{S}$ is contained in the reflection plane. The scalar product with the normal vector $\mathbf{n}$ produces a scalar field characterizing the magnitude of the S-mode, but signed according to its relation to the normal $\mathbf{n}$. This scalar quantity can be correlated with the scalar reflected P wavefield, thus leading to a scalar image without sign change as a function of the incidence direction. Therefore, SP images

Downloaded 08/11/16 to 138.67.12.184. Redistribution subject to SEG license or copyright; see Terms of Use at http://library.seg.org/

produced in this fashion can also be stacked without canceling each other at various positions in space.

In 2D, the scalar imaging conditions from equations 4 and 5 are simplified. The **S** has only one nonzero component S_y because the vector **S** is orthogonal to the local reflection plane $\mathcal{R}$. Therefore, the PS and SP imaging conditions are

$$I^{PS} = -\sum_e \sum_t \left(\frac{\partial P}{\partial x} n_z - \frac{\partial P}{\partial z} n_x \right) S_y, \tag{6}$$

$$I^{SP} = \sum_e \sum_t \left(\frac{\partial S_y}{\partial x} n_z - \frac{\partial S_y}{\partial z} n_x \right) P, \tag{7}$$

where $I{=}I(x,z)$, $P = P(e,x,z,t)$, $S_y = S_y(e,x,z,t)$, $n_z = n_z(x,z)$ and $n_x = n_x(x,z)$. For a horizontal reflector, i.e., $\mathbf{n} = \{0,0,1\}$, we can write

$$I^{\mathrm{PS}} = -\sum_e \sum_t \frac{\partial P}{\partial x} S_y, \tag{8}$$

$$I^{\mathrm{SP}} = \sum_e \sum_t \frac{\partial S_y}{\partial x} P, \tag{9}$$

which indicates that in the scalar imaging condition, we correlate the P or S wavefields with the x derivative of the S or P wavefields, respectively. That is, of course, just a special case of the more general relation in equations 4 and 5.

We interpret the propagation direction of the P-mode and the polarization direction of the S-mode as the gradient and curl of the displacement vector field, respectively. For a plane wave, ∇P and $\nabla \times \mathbf{S}$ are equivalent to $i\mathbf{k}P$ and $i\mathbf{k} \times \mathbf{S}$, respectively, where **k** is the wavenumber vector indicating the propagation direction. However, although the spatial derivatives contained in the gradient and curl provide information regarding the directionality of the wavefield, the application of the gradient and curl operators also distorts the amplitude spectrum as well as the phase of the wavefield, and implicitly it distorts the phase of the migrated images. The distortion of the amplitude and phase is undesirable and must be avoided because it can lead to incorrect stratigraphic interpretation.

To correct for a similar distortion of images resulting from the application of a Laplacian filter designed to remove backscattering artifacts in RTM, Zhang and Sun (2009) apply a v^2/ω^2 filter that compensates for the k^2 representing the Laplacian. Here, v is velocity and ω is the angular frequency. To apply this filter, Zhang and Sun (2009) propose a two-step approach: First, divide the source function by ω^2 prior to reconstructing the source wavefield, and second, scale the image by v^2 following migration. The ω^2 filtering is equivalent to a double-time integral. We follow their approach and use a similar filter to correct for the distortion of the amplitude and phase of the image. Notice that we can write $i\mathbf{k} = \frac{i\omega}{v}\frac{\mathbf{k}}{|\mathbf{k}|}$, where the unit vector $\frac{\mathbf{k}}{|\mathbf{k}|}$ is the propagation direction. Hence, to correct the imaging condition in equation 4, we apply a $1/i\omega$ filter by integrating the source function over time prior to source wavefield reconstruction, and then we multiply the image in the space domain by the P-wave velocity v. A similar transformation is applicable for the imaging condition in equation 5 except that in this case, we scale by the S-wave velocity.

Figure 4a shows a 1D image obtained by crosscorrelation of the source and receiver wavefields. After applying a gradient filter, which is a spatial derivative in 1D, the amplitude and phase of the image change (Figure 4b). To allow for application of the gradient filter while preserving the amplitude and phase, we follow the flow discussed above to obtain the image shown in Figure 4c, which is identical to the image shown in Figure 4a.

Using the same $v/(i\omega)$ filter, we are also able to correct for the amplitude and phase distortion resulting from Helmholtz decomposition, which involves computation of the divergence and curl of the displacement wavefields. In this case, we apply the filter $v/(i\omega)$ to the source and receiver wavefields except that the meaning of the velocity is different, depending on whether we operate with the P- or S-mode. Similar to the correction for our proposed imaging condition, we apply a $1/i\omega$ filter by integrating over time the source function prior to the source wavefield reconstruction and by integrating the recorded data prior to receiver wavefield reconstruction. Then, we multiply the PS and SP images by the product of the velocities for the source and receiver wavefields.

In summary, to correct for the amplitude and phase distortion resulting from the Helmholtz decomposition and the scalar imaging condition, we combine the two corrections discussed earlier by (1) integrating the source function over time twice, prior to source wavefield reconstruction, (2) integrating the recorded data over time once, prior to receiver wavefield reconstruction, and (3) multiplying the PS image by $v_p^2 v_s$ and the SP image by $v_p v_s^2$.

The units of the original displacement wavefield are meters, and the units of the spatial derivative of the wavefield are 1. The application of a $v/(i\omega)$ filter, to correct for the amplitude and phase

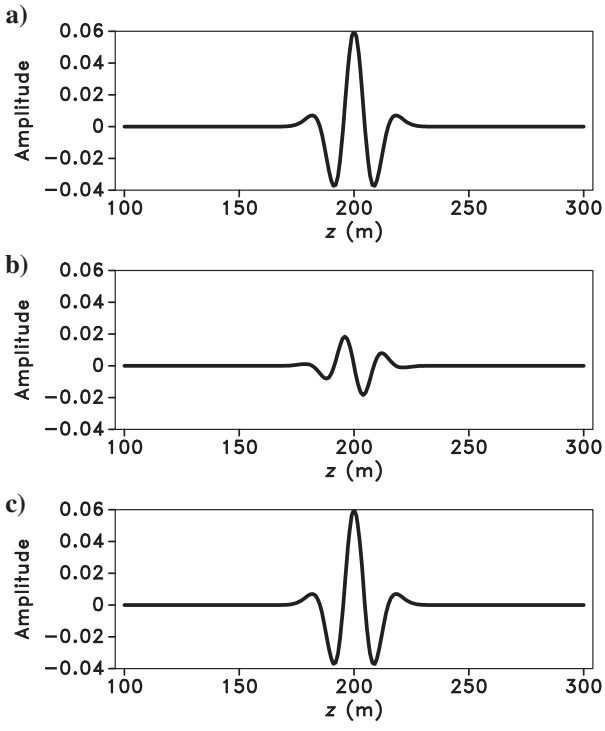


Figure 4. One-dimensional images obtained by (a) crosscorrelation of source and receiver wavefields, (b) crosscorrelation followed by the spatial derivative, and (c) source integral prior to crosscorrelation, followed by the spatial derivative.

Downloaded 08/11/16 to 138.67.12.184. Redistribution subject to SEG license or copyright; see Terms of Use at http://library.seg.org/

distortion caused by the spatial derivative, changes the units of the spatial derivative of the wavefield back to meters. Therefore, the units of the image computed from the new imaging condition with the filter are meters squared.

For the 3D example in Figure 1a, the scalar imaging condition leads to the PS image in Figure 5. In this figure, we apply the filters to correct for image spectrum and amplitude distortions due to Helmholtz decomposition and the scalar imaging condition. In contrast to the vector PS image characterized by polarity reversal obtained by using the conventional imaging condition, the PS image obtained using the scalar imaging condition is a scalar without polarity reversal. This correction allows us to stack multiple elastic images over experiments without cancellation due to opposite polarity of the images constructed from different experiments.

EXAMPLES

We illustrate our method using three synthetic models. During the procedure for obtaining PS and SP images, we apply the filters to correct for the amplitude and phase distortion. In the first two examples, we also add a thin water layer to both of the models to generate PS conversion from a hard water bottom. The water layer is 0.4 km. The models are smoothed for source and receiver wavefield reconstruction. The first model (Figure 6) consists of semiparallel gently dipping layers. We use 40 sources evenly distributed along the surface and 500 receivers located at the surface of the model. The source function is a Ricker wavelet with a peak frequency of 35 Hz. Figure 7a and 7b are snapshots of the source P- and receiver S-wavefields, respectively, and Figure 8a and 8b are snapshots of the source S- and receiver P-wavefields, respectively. In both cases, we observe polarity flips in the S-wavefield.

Using the conventional imaging condition (i.e., crosscorrelation of the source and receiver wavefields), we obtain the PS and SP image shown in Figures 9a and 10a. The reflectors on the left side of the model are not well-imaged, due to the fact that the polarity of individual images change sign at normal incidence, thus causing destructive interference during summation over shots. The PS and SP common image gathers at $x = 1.5$ km (Figures 11a and 12a) show this polarity reversal causing image destruction.

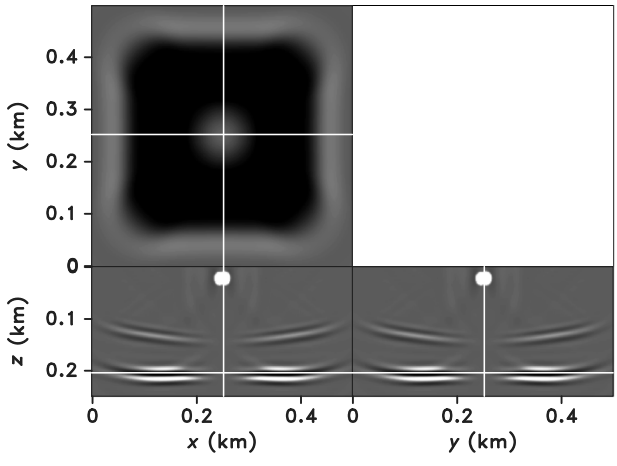


Figure 5. The PS image computed using the scalar imaging condition. Compared with the three components of the vector image shown in Figure 2b, 2d, and 2f, this PS image is a scalar without polarity reversal.

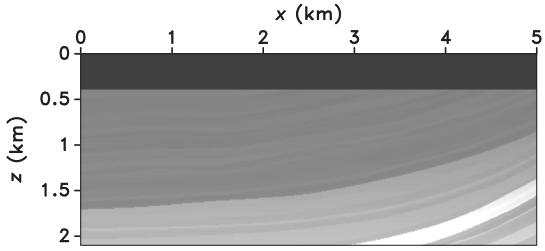


Figure 6. 2D synthetic density model with dipping layers.

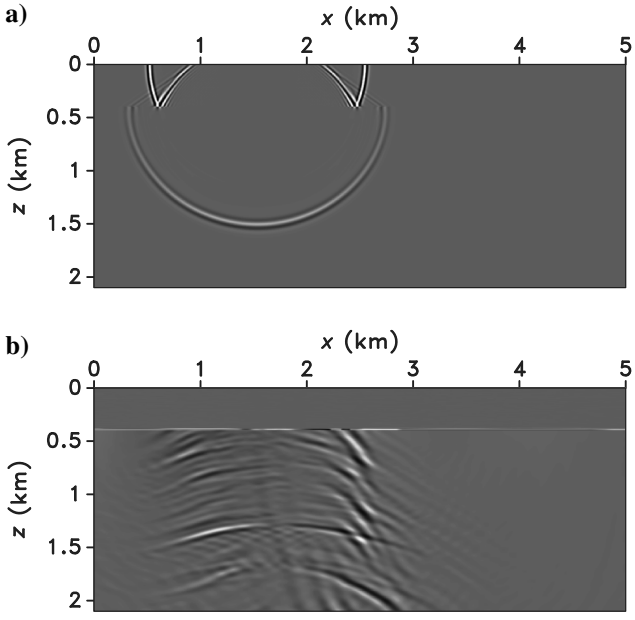


Figure 7. (a) Source P-wavefield and (b) receiver S-wavefield for a single shot. The source and receivers are on the surface of the model.

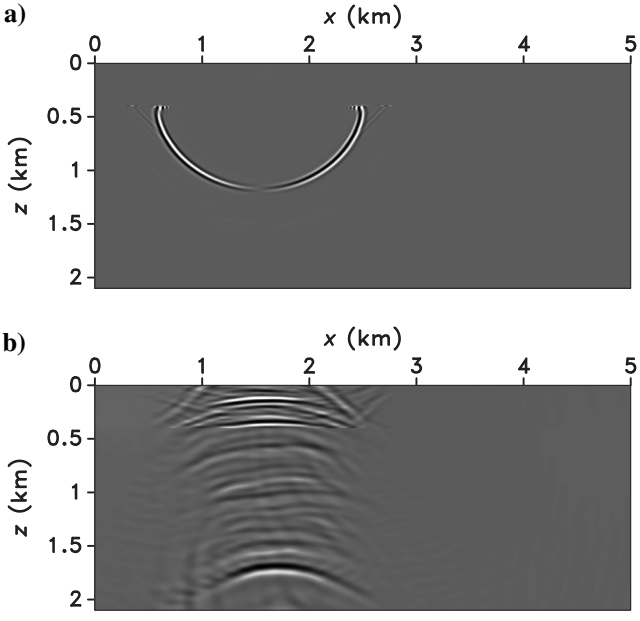


Figure 8. (a) Source S-wavefield and (b) receiver P-wavefield for a single shot. The source and receivers are on the surface of the model.

Downloaded 08/11/16 to 138.67.12.184. Redistribution subject to SEG license or copyright; see Terms of Use at http://library.seg.org/

In contrast, Figures 9b and 10b show PS and SP images using the scalar imaging condition, respectively. In this case, the interfaces are more continuous compared with the image constructed by the simple crosscorrelation imaging condition. Moreover, the PS and SP common image gathers at $x = 1.5$ (Figures 11b and 12b) confirm that there is no polarity change as a function of shot position.

The second example (Figure 13) is a modified Marmousi model (Versteeg, 1991, 1993). It contains several major faults and semiparallel dipping layers. We use 60 explosive sources evenly distributed along the surface, and receivers are on a cable that moves with the source. The source-receiver offset ranges from −1.5 to 1.5 km.

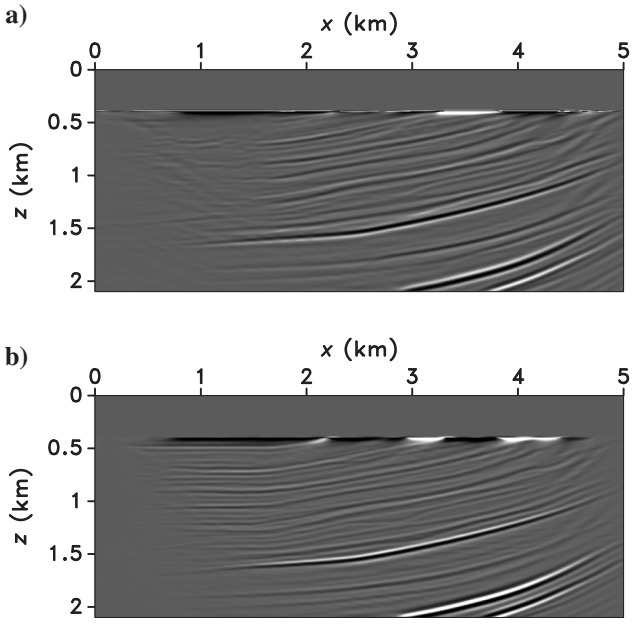


Figure 9. PS stacked images obtained using (a) the conventional imaging condition and (b) the scalar imaging condition. The image in panel (b) at (1.0, 1.0) km is stronger, in contrast with the image in panel (a), which suffers from cancellation due to polarity reversal.

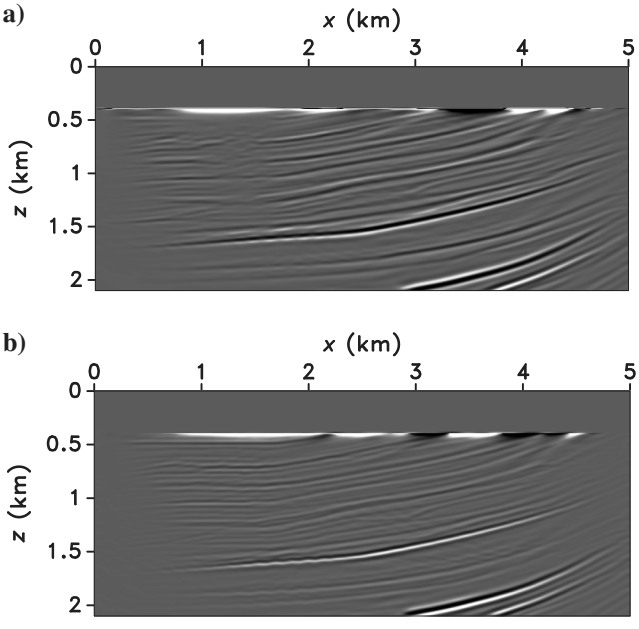


Figure 10. SP images obtained using (a) the conventional imaging condition and (b) the scalar imaging condition. The image in panel (b) at (0, 0.7) km is stronger, in contrast with the image in panel (a), which suffers from cancellation due to polarity reversal.

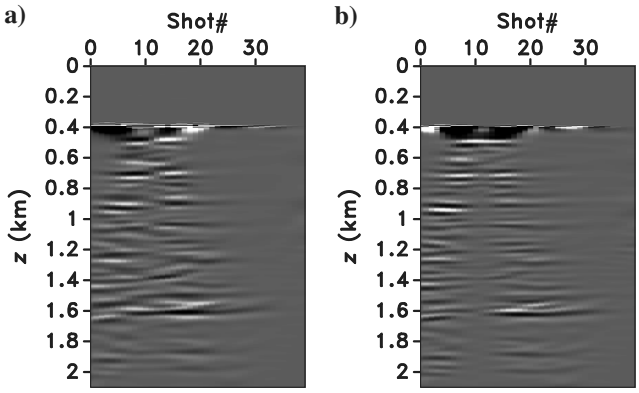


Figure 11. PS common image gather at $x = 1.5$ km obtained from (a) the conventional imaging condition. From left to right, the horizontal events change sign at normal incidence. (b) Using the scalar imaging condition, we obtain the PS common image gather without polarity change.

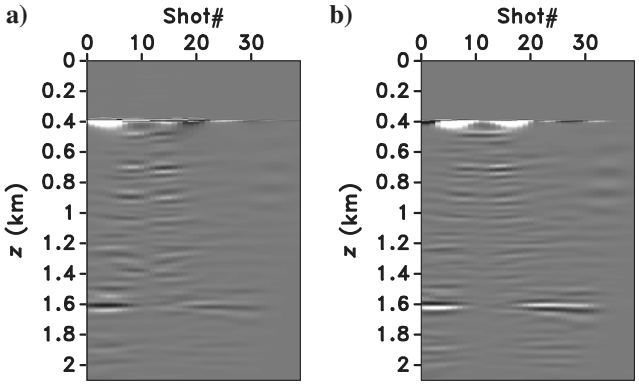


Figure 12. SP common image gather at $x = 1.5$ km obtained from (a) the conventional imaging condition. From left to right, the horizontal events change sign at normal incidence. (b) Using the scalar imaging condition, we obtain the SP common image gather without polarity changes.

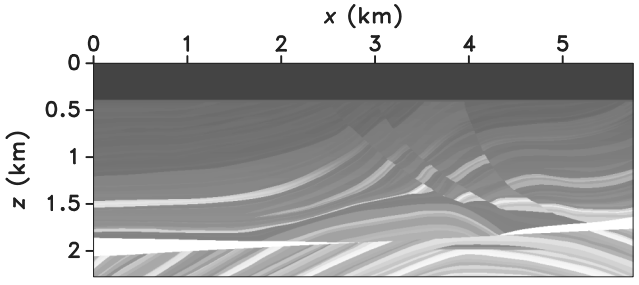


Figure 13. Marmousi model with density contrast.

The source function is a Ricker wavelet with a peak frequency of 35 Hz.

The source S wavefield is weak because of the minor energy conversion at the top of the model; therefore, the SP image is also weak. Consequently, in the figures, we show only the PS image. Using the conventional imaging condition, we obtain an image from a single shot and the stacked PS image shown in Figures 15a and 16a, respectively. One common image gather (Figure 14a), is extracted from all 60 experiments at $x = 2.5$ km. In Figures 16a and 14a, the events change polarity at normal incidence, which leads to destructive interference in the stacked image. The simplest correction is to change the sign of the image where the offset is negative. One common image gather at $x = 2.5$ km and one image from a single shot are shown in Figure 14b and Figure 15b, respectively. This method corrects for polarity change at a large offset, but it does not work at small incidence angles. The stacked image seen in Figure 16b is better focused than the image in Figure 16a; however, the middle part with complicated geologic structures is not well-illuminated. By applying the new imaging condition, we obtain the common image gathers and the image from a single shot without polarity reversal shown in Figure 14c and 15c, respectively. Notice that in the stacked image shown in Figure 16c, events are well-focused.

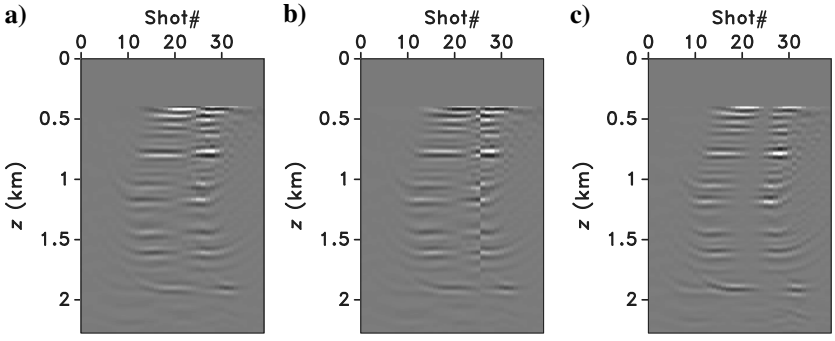


Figure 14. PS common image gather at $x = 2.5$ km obtained from (a) the conventional imaging condition, (b) the conventional imaging condition with the simple correction that flips the sign of the image at negative offset, and (c) the scalar imaging condition.

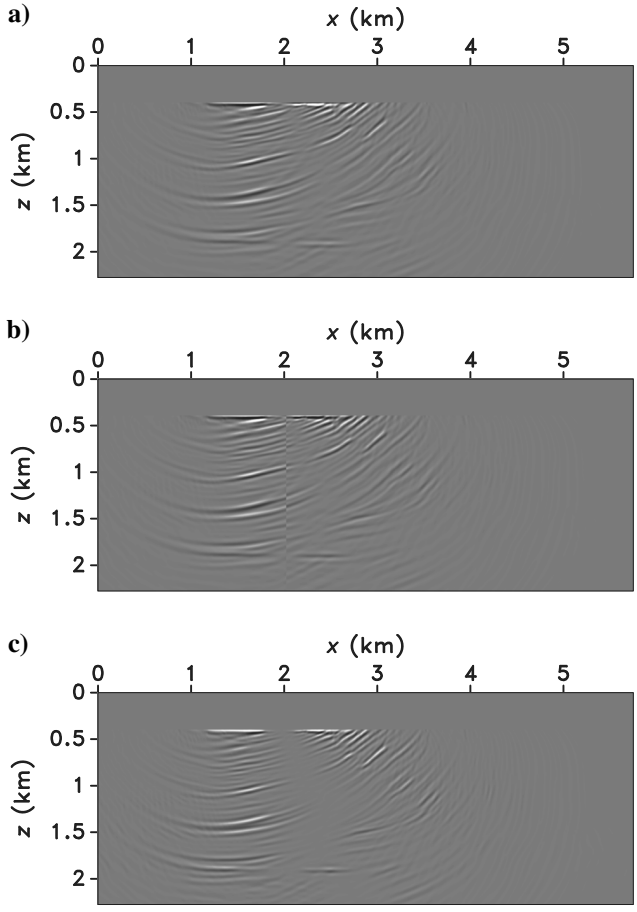


Figure 15. PS image from a single shot using (a) the conventional imaging condition, (b) the conventional imaging condition with simple correction that flips the sign of the image at negative offset, and (c) the scalar imaging condition. The source is located at (1.85, 0) km.

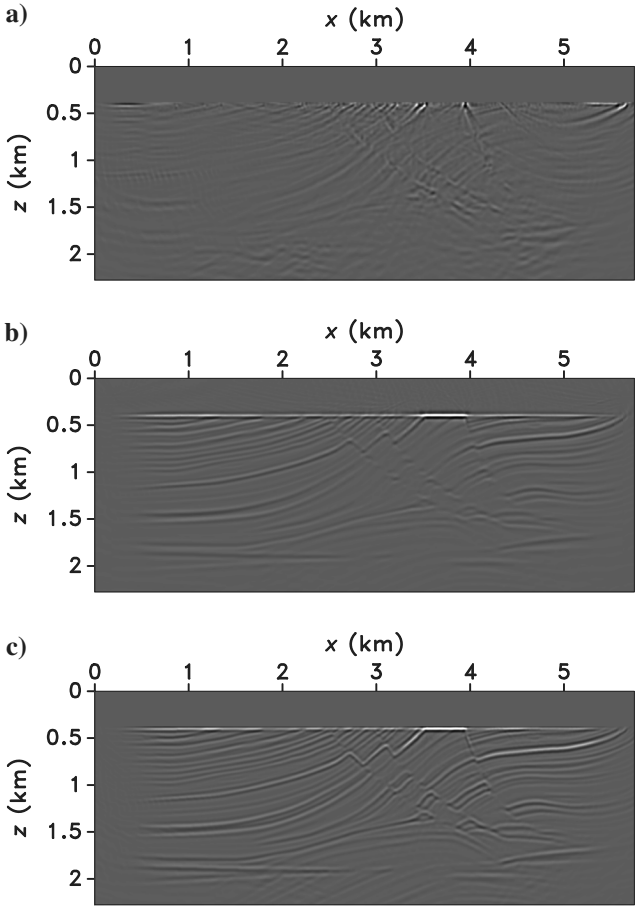


Figure 16. PS stacked image using (a) the conventional imaging condition, (b) the conventional imaging condition with simple correction that flips the sign of the image at negative offset, and (c) the scalar imaging condition.

Downloaded 08/11/16 to 138.67.12.184. Redistribution subject to SEG license or copyright; see Terms of Use at http://library.seg.org/

Downloaded 08/11/16 to 138.67.12.184. Redistribution subject to SEG license or copyright; see Terms of Use at http://library.seg.org/

The third model is the 3D SEG/EAGE salt model (Aminzadeh et al., 1997), and the density model is shown in Figure 17a. The P and S velocity models are smoothed. We use nine sources evenly distributed in a horizontal plane at $z = 0.02$ km and a dense network of receivers at $z = 0.03$ km. We simulate the data with contrasts in the density model and use displacement vectors at the receiver locations as recorded data. The source function is represented by a Ricker wavelet with a peak frequency of 40 Hz. Using the scalar imaging condition, we obtain the PS stacked image, Figure 17b. In the PS image, the salt boundary is continuous without polarity change, which shows that the scalar imaging condition works for 3D cases with complicated geologic structures.

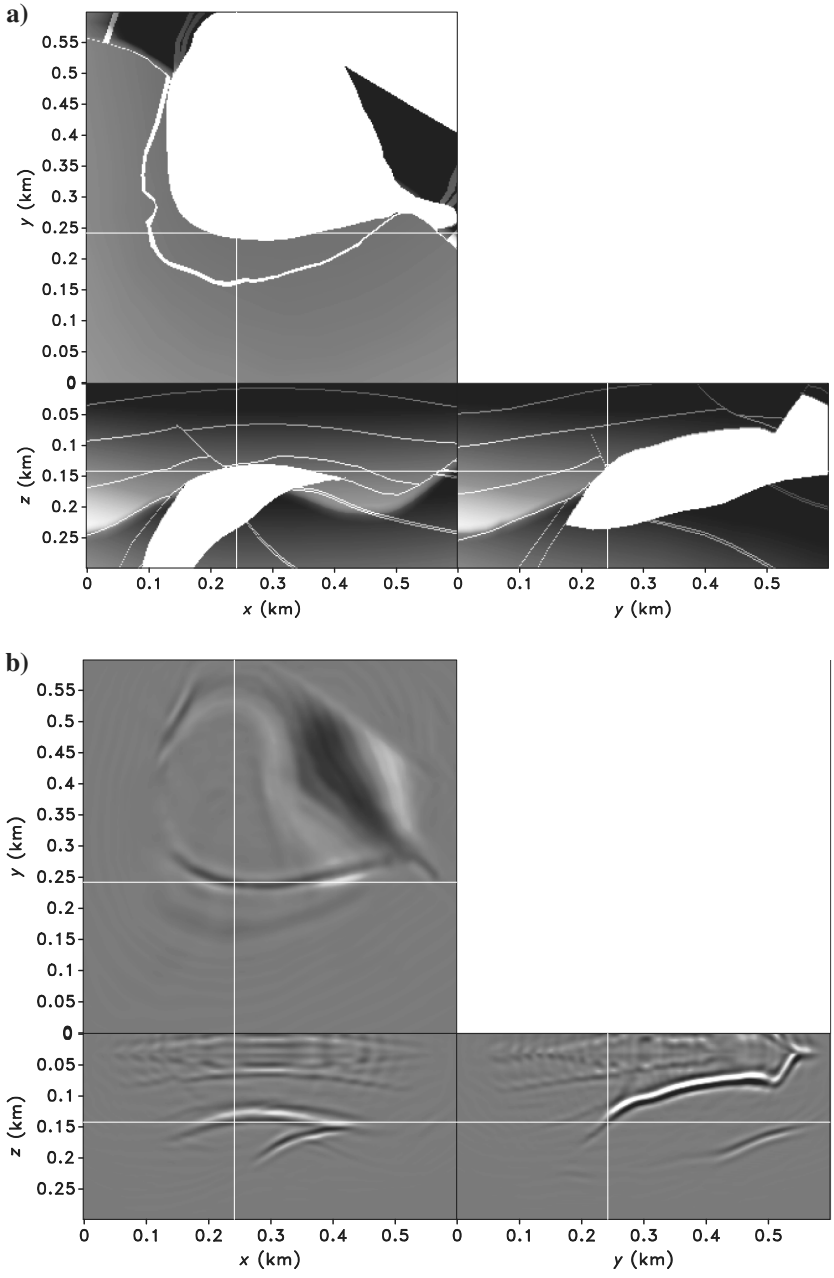


Figure 17. (a) 3D SEG/EAGE salt model, the density model. (b) The PS image obtained using the scalar imaging condition.

CONCLUSIONS

We derive a new 3D imaging condition for PS and SP images constructed by elastic RTM. In conventional methods, P- and S-modes are obtained using Helmholtz decomposition. However, our imaging condition does not correlate various components of the S wavefield with the P wavefield; instead, our method uses geometric relationships between the wavefields, their propagation directions, and the reflector orientation and polarization directions to construct a single scalar image characterizing the PS or SP reflectivity. Our method leads to accurate images without the need to decompose wavefields into directional components or to construct costlier extended images in the angle domain. However, our method is constructed based on the assumption that the polarity changes at normal incidence in isotropic media. In the case of anisotropy, the polarity may change at a nonzero incidence angle, in which case, the imaging condition would need to be modified.

ACKNOWLEDGMENTS

We thank the sponsor companies of the Consortium Project on Seismic Inverse Methods for Complex Structures, whose support made this research possible. The reproducible numeric examples in this paper use the Madagascar open-source software package (Fomel et al., 2013) freely available from http://www.ahay.org. The authors thank Tariq Alkhalifah for helpful discussions and valuable suggestions.

REFERENCES

Aki, K., and P. Richards, 2002, Quantitative seismology, 2nd ed.: University Science Books.

Aminzadeh, F., J. Brac, and T. Kunz, 1997, 3-D salt and overthrust models: SEG.

Artman, B., I. Podladtchikov, and A. Goertz, 2009, Elastic time-reverse modeling imaging conditions: 79th Annual International Meeting, SEG, Expanded Abstracts, 1207–1211.

Balch, A. H., and C. Erdemir, 1994, Sign-change correction for prestack migration of P-S converted wave reflections: Geophysical Prospecting, **42**, 637–663, doi: 10.1111/j.1365-2478.1994.tb00233.x.

Claerbout, J. F., 1971, Toward a unified theory of reflector mapping: Geophysics, **36**, 467–481, doi: 10.1190/1.1440185.

Dellinger, J., and J. Etgen, 1990, Wavefield separation in two-dimensional anisotropic media: Geophysics, **55**, no. 7, 914–919, doi: 10.1190/1.1442906.

Denli, H., and L. Huang, 2008, Elastic-wave reverse-time migration with a wavefield-separation imaging condition: 78th Annual International Meeting, SEG, Expanded Abstracts, 2346–2350.

Dickens, T. A., and G. A. Winbow, 2011, RTM angle gathers using Poynting vectors: 81st Annual International Meeting, SEG, Expanded Abstracts, 3109–3113.

Du, Q., X. Gong, Y. Zhu, G. Fang, and Q. Zhang, 2012a, PS wave imaging in 3D elastic reverse-time migration: 82nd Annual International Meeting, SEG, Expanded Abstracts, doi: 10.1190/segam2012-0107.1.

Du, Q., Y. Zhu, and J. Ba, 2012b, Polarity reversal correction for elastic reverse time migration: Geophysics, **77**, no. 2, S31–S41, doi: 10.1190/geo2011-0348.1.

Duan, Y., and P. C. Sava, 2014, Elastic reverse-time migration with OBS multiples: 84th Annual

International Meeting, SEG, Expanded Abstracts, 4071–4076.
Fomel, S., P. Sava, I. Vlad, Y. Liu, and V. Bashkardin, 2013, Madagascar: Open-source software project for multidimensional data analysis and reproducible computational experiments: Journal of Open Research Software, **1**, e8, doi: http://dx.doi.org/10.5334/jors.ag.
Patrikeeva, N., and P. Sava, 2013, Comparison of angle decomposition methods for wave-equation migration: 83rd Annual International Meeting, SEG, Expanded Abstracts, 3773–3778.
Rosales, D. A., S. Fomel, B. L. Biondi, and P. C. Sava, 2008, Wave-equation angle-domain common-image gathers for converted waves: Geophysics, **73**, no. 1, S17–S26, doi: 10.1190/1.2821193.
Sun, R., G. A. McMechan, C. Lee, J. Chow, and C. Chen, 2006, Prestack scalar reverse-time depth migration of 3D elastic seismic data: Geophysics, **71**, no. 5, S199–S207, doi: 10.1190/1.2227519.
Versteeg, R., 1991, Analysis of the problem of the velocity model determination for seismic imaging: Ph.D. thesis, University of Paris VII.
Versteeg, R., 1993, Sensitivity of prestack depth migration to the velocity model: Geophysics, **58**, 873–882, doi: 10.1190/1.1443471.
Wu, R., R. Yan, and X. Xie, 2010, Elastic converted-wave path migration for subsalt imaging: 80th Annual International Meeting, SEG, Expanded Abstracts, 3176–3180.
Yan, J., and P. Sava, 2008, Isotropic angle-domain elastic reverse-time migration: Geophysics, **73**, no. 6, S229–S239, doi: 10.1190/1.2981241.
Yan, R., and X. Xie, 2012, An angle-domain imaging condition for elastic reverse time migration and its application to angle gather extraction: Geophysics, **77**, no. 5, S105–S115, doi: 10.1190/geo2011-0455.1.
Yoon, K., K. Marfurt, and E. W. Starr, 2004, Challenges in reverse-time migration: 74th Annual International Meeting, SEG, Expanded Abstracts, 1057–1060.
Zhang, Y., and J. Sun, 2009, Practical issues in reverse time migration: True amplitude gathers, noise removal and harmonic source encoding: First Break, **27**, 29–35, doi: 10.3997/1365-2397.2009002.

Downloaded 08/11/16 to 138.67.12.184. Redistribution subject to SEG license or copyright; see Terms of Use at http://library.seg.org/